



Observations of the Orion Source I Disk and Outflow Interface

Melvyn Wright¹, Richard Plambeck¹, Tomoya Hirota², Adam Ginsburg³, Brett McGuire³, John Bally⁴, and Ciriaco Goddi⁵

¹Radio Astronomy Lab, University of California, 501 Campbell Hall, Berkeley, CA 94720-3441, USA

²Mizusawa VLBI Observatory, National Astronomical Observatory of Japan, Osawa 2-21-1, Mitaka, Tokyo 181-8588, Japan

³National Radio Astronomy Observatory, Charlottesville, VA 22903, USA

⁴CASA, University of Colorado, 389-UCB, Boulder, CO 80309, USA

⁵Leiden Observatory, Leiden University, P.O. Box 9513, 2300 RA Leiden, The Netherlands

Received 2019 September 14; revised 2019 November 14; accepted 2019 November 16; published 2020 February 3

Abstract

We imaged the continuum and molecular line emission from Orion Source I (SrcI) with up to 30 mas (12 au) resolution at 43, 99, 223, and 340 GHz in an attempt to probe the structure and chemistry of the circumstellar disk and bipolar outflow associated with this high-mass protostar. The continuum spectral index ranges from ~ 2 along the midplane of the disk to ~ 3 along the edges, consistent with dust that is optically thick in the midplane but becomes optically thin at the periphery. Salt (NaCl) emission is visible where the dust is optically thin; it provides a unique tracer of the velocity field within the disk. All other molecules that we have mapped—H₂O, AlO, SiO, SiS, SO, and SO₂—appear to originate primarily in the bipolar outflow. The base of the outflow is corotating with the disk. SiS shows a filamentary structure that is most prominent along the edges of the outflow. The molecular distributions suggest that Si and Al released from dust grains in the disk react with oxygen derived from H₂O to form SiO and AlO, and with SO and SO₂ to form SiS.

Unified Astronomy Thesaurus concepts: Protostars (1302); Circumstellar disks (235); Molecular gas (1073); Astrochemistry (75)

1. Introduction

The Kleinmann–Low Nebula in Orion, at a distance of 415 pc (Menten et al. 2007; Kim et al. 2008; Kounkel et al. 2018), is the nearest interstellar cloud in which massive ($M > 8 M_{\odot}$) stars are forming. The two most massive stars in this region, Source I (SrcI) and the Becklin–Neugebauer Object (BN), appear to be recoiling from one another at 35–40 km s^{−1} (Rodríguez et al. 2005; Gómez et al. 2008; Goddi et al. 2011b), suggesting that they were ejected from a multiple system via dynamical decay approximately 500 yr ago (Bally et al. 2017). SrcI has a mass $\sim 15 M_{\odot}$ (Ginsburg et al. 2018), with a rotating accretion disk and a molecular outflow that is prominent in SiO. The disk around SrcI has been studied as it is the closest known disk around a high-mass protostar (Hirota et al. 2014; Plambeck & Wright 2016; Ginsburg et al. 2018); it is associated with SiO and H₂O masers (Reid et al. 2007; Goddi et al. 2009, 2011b; Plambeck et al. 2009; Matthews et al. 2010; Niederhofer et al. 2012; Greenhill et al. 2013). Recently, dozens of spectral lines of NaCl and KCl were identified in this disk (Ginsburg et al. 2019). The rich chemistry of SrcI’s disk and outflow raises the question of whether this source is a paradigm for high-mass star formation, or an anomaly born in the unique environment created by the SrcI/BN interaction and associated explosive outflow (Bally et al. 2017).

In this paper, we present high-resolution images of SrcI that were made from Karl G. Jansky Very Large Array (VLA) and Atacama Large Millimeter/submillimeter Array (ALMA) data at 43, 99, 223, and 340 GHz. We use continuum images with 30 mas (12 au) resolution to probe the dust opacity across the disk. We discuss chemical pathways that can lead to the observed molecular distributions.

2. Observations and Data Reduction

Table 1 provides a summary of the observations, including project codes.

2.1. 43 GHz

The spectral setup for the 43 GHz VLA observations included 16 wideband windows, each covering 116 MHz bandwidth and 58 spectral channels. The VLA wideband setup is 64 channels covering 128 MHz; the reduction script trimmed off end channels because of analog filter rolloff. The data were self-calibrated using a strong SiO $v = 1, J = 1 - 0$ maser feature at -3.5 km s^{−1} that was observed simultaneously in a narrowband window with a spectral resolution of 0.3 km s^{−1}.

The wideband average, with a mean frequency of 42.65 GHz and a bandwidth of 1.4 GHz, excludes four spectral windows containing spectral line emission. We made images with the synthesized beamwidth of 56×44 mas, and convolved to 30 and 50 mas resolution for comparison with images at 99 GHz (see below).

2.2. 99 GHz

ALMA observations at 99 GHz (Band 3; B3) on 2017 October 12 and 17 included four spectral windows, each with a bandwidth of 1.875 GHz and 960 spectral channels. The wideband average with a mean frequency of 99.275 GHz and a bandwidth of 7.5 GHz excludes channels containing spectral line emission. The data were calibrated using observatory-supplied scripts. We made images with the synthesized beamwidth 45×36 mas, and convolved to 30 and 50 mas resolution for comparison with images at 43 GHz.

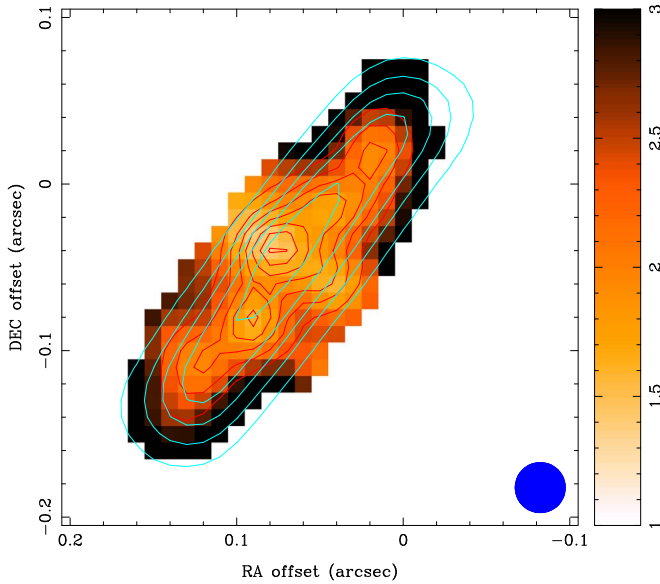
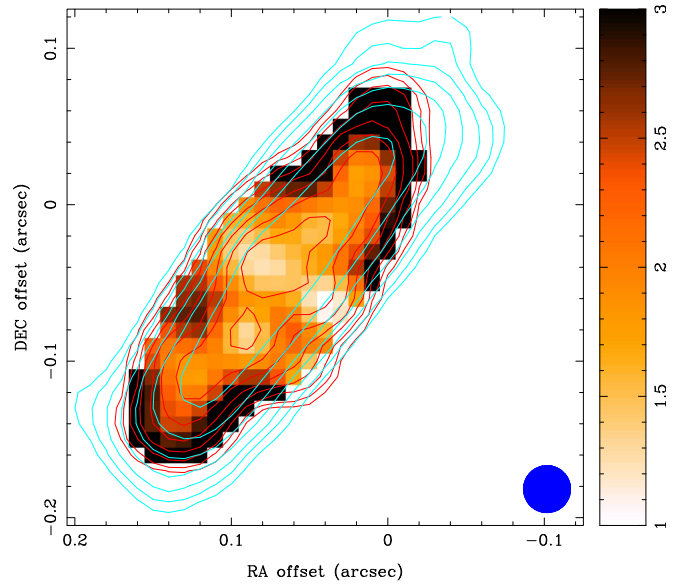
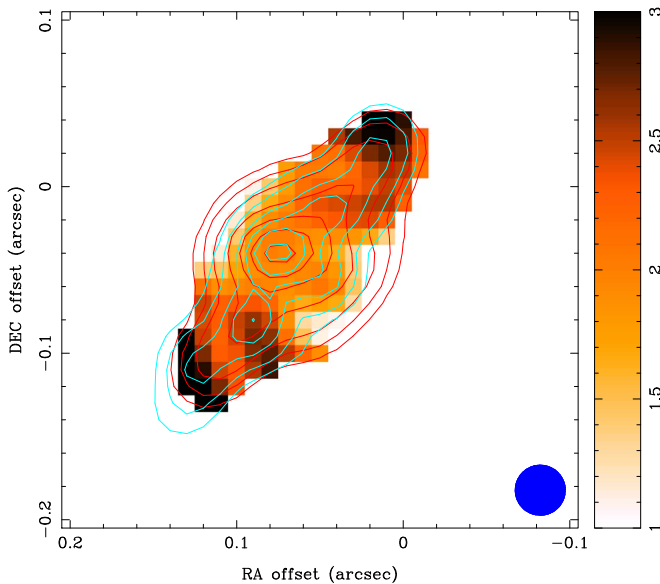
2.3. 223 and 340 GHz

The 223 GHz (ALMA Band 6; B6) and 340 GHz (ALMA Band 7; B7) observations and calibration are described in Ginsburg et al. (2018). These data were not self-calibrated. The observational parameters are given in Table 1.

In order to compare the SrcI outflow with the large-scale structure associated with the SrcI/BN explosion mapped in CO

Table 1
Observations

Frequency (GHz)	Project Code	Date	Time (minutes)	Synth Beam (milliarcsec)	Baseline (m)
43	VLA/18A-136	2018 Mar 6	291	56×44 at PA 33	500–36,600
99	2017.1.00497.S	2017 Oct 12	158	45×36 at PA 47	40–16,200
216–220	2013.1.005446.S	2014 Dec to 2015 Apr	15	1500×930 at PA -8	14–330
224	2016.1.00165.S	2017 Sep 19	44	39×19 at PA 66	40–10,500
340	2016.1.00165.S	2017 Nov 8	45	26×11 at PA 58	90–12,900
350	2012.1.00123.S	2014 Jul 26	24	276×260 at PA 85	30–730

**Figure 1.** Spectral index from 99–340 GHz. The red contour levels at 99 GHz: 200, 400, 600, 800, 1000, 1200, 1400 K. The blue contour levels at 340 GHz: 100, 200, 300, 400, 500, 600 K. The color image shows the spectral index distribution. The 30 mas convolving beam FWHM is indicated in blue in the lower right.**Figure 3.** Spectral index from 99–223 GHz. The red contour levels at 99 GHz: 5, 10, 20, 40, 80, 160, 320, 640 K. The blue contour levels at 223 GHz: 5, 10, 20, 40, 80, 160, 320, 640 K. The color image shows the spectral index distribution. The 30 mas convolving beam FWHM is indicated in blue in the lower right.**Figure 2.** Spectral index from 43–99 GHz. The red contour levels at 43 GHz: 200, 400, 600, 800, 1000, 1200, 1400 K. The blue contour levels at 99 GHz: 100, 200, 300, 400, 500, 600 K. The color image shows the spectral index distribution. The 30 mas convolving beam FWHM is indicated in blue in the lower right.

by Bally et al. (2017), we imaged other spectral lines that fell within the passband of these lower-resolution observations (ADS/JAO.ALMA#2013.1.00546.S). The data were calibrated using the observatory-supplied CASA scripts. We made mosaic images from these data in a $30''$ field around Src1 in SO, SO_2 , and SiO emission with $1.5 \times 0''.9$ angular and 2 km s^{-1} velocity resolution. We used only the ALMA 12 m array data in these images to filter out the large-scale structure and enhance the filamentary structures.

The MIRIAD software package (Sault et al. 1995) was used to image and analyze all the data in this paper.

3. The Src1 Disk

We used both the CLEAN and Maximum Entropy algorithms to image the JVLA and ALMA data. We convolved the continuum images to a common resolution of 30 mas and 50 mas resolution in order to make spectral index images between 43, 99, 223 and 340 GHz. Because the 43 GHz data were self-calibrated, the wideband image was spatially offset from the higher-frequency images. We aligned the 43 GHz image with the 99 GHz image using the MIRIAD task *indiff*, which finds optimum parameters in a maximum likelihood sense for making one image approximate another image. The parameters adjusted were shifts 9 mas in R.A. and -2 mas in decl. to an image center at R.A. = 05:35:14.513, decl. = $-05:22:30.576$ used in the

Table 2
Measured Sizes and Flux Densities for Source I

Frequency (GHz)	Beam (arcsec, PA)	Deconvolved Size (arcsec, PA)	Integrated Flux (mJy)
43	$0.06 \times 0.04, 33^\circ$	$0.099 \pm 0.002 \times 0.057 \pm 0.002, -40^\circ4 \pm 2^\circ7$	10 ± 1
99	$0.04 \times 0.04, 47^\circ$	$0.151 \pm 0.005 \times 0.044 \pm 0.002, -37^\circ8 \pm 1^\circ3$	58 ± 6
224	$0.04 \times 0.02, 66^\circ$	$0.197 \pm 0.003 \times 0.042 \pm 0.003, -37^\circ3 \pm 0^\circ4$	256 ± 25
340	$0.03 \times 0.01, 58^\circ$	$0.234 \pm 0.005 \times 0.042 \pm 0.002, -37^\circ4 \pm 0^\circ3$	630 ± 63

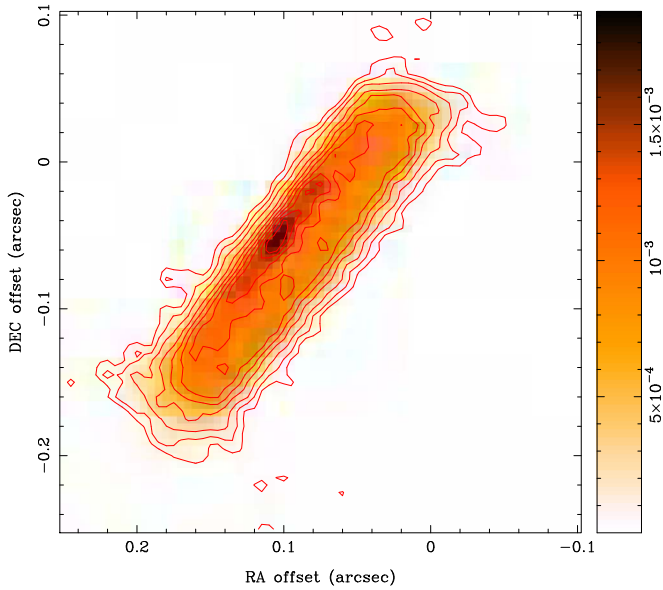


Figure 4. 340 GHz continuum emission. Maximum entropy image with 5 mas pixels. Contours are at 25, 50, 100, 200, 300, 400, 500, 600, 700, and 800 K. The linear color scale is in units of Jy pixel^{-1} (480 K mJy^{-1}). The peak brightness at the compact source is 874 K.

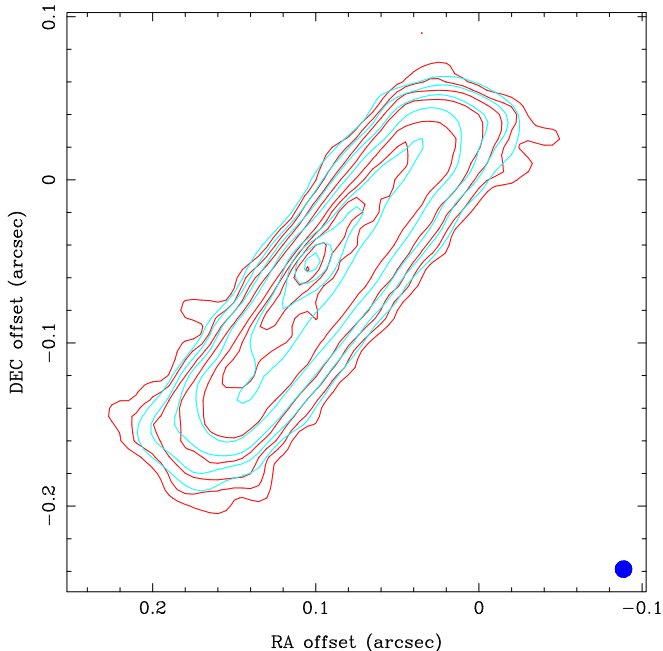


Figure 5. Comparison of the maximum entropy images at 340 GHz and 223 GHz convolved with a 10 mas beam shown in the lower right. Contours are at 25, 50, 100, 200, 300, 400, 500, 600, 700, and 800 K.

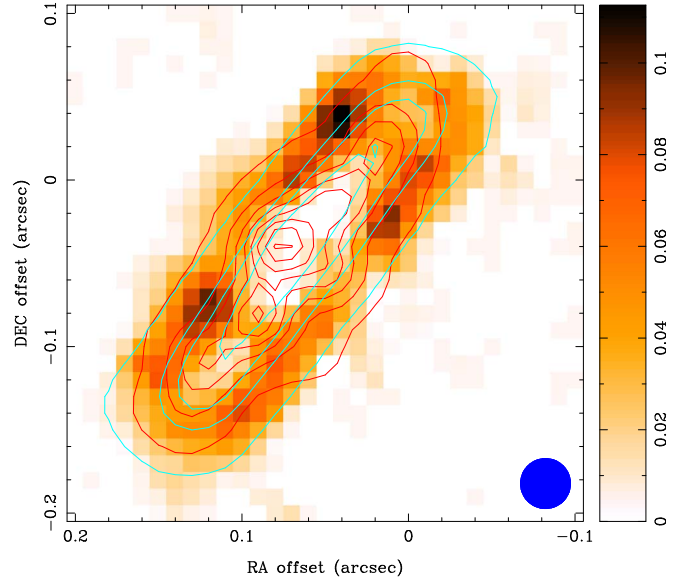


Figure 6. NaCl emission at 232.51 GHz integrated over a velocity range of $(-30 \text{ to } 30) \text{ km s}^{-1}$. The red contour levels at 99 GHz: 25, 200, 400, 600, 800, 1000, 1200, 1400 K. The blue contour levels at 340 GHz: 25, 200, 300, 400, 500, 600 K. The color image shows the NaCl distribution. The 30 mas convolving beam FWHM is indicated in blue in the lower right.

following figures. The 99, 223, and 340 GHz data were not self-calibrated, only the 43 GHz image position was adjusted. SrcI is moving at $Dx = 6.3, Dy = -4.2 \text{ mas yr}^{-1}$ (Goddi et al. 2011b). The 99, 223, and 340 GHz image data were acquired within a ~ 2 month period (see Table 1) and the offset in the images from the proper motion is less than $\sim 0.4 \text{ au}$.

3.1. Spectral Index Distribution

Figures 1–3 show the spectral index computed from the ratio of continuum brightness at 340, 223, 99, and 43 GHz at 30 mas resolution. At 50 mas resolution, the same spectral index distributions are seen, convolved to the lower resolution. The rms noise levels on the continuum images are 4 K, 3 K, 7 K, and 6 K, respectively; the images were clipped at 5% of the peak for the spectral index calculation. The figures show that the spectral index is ~ 2 along the midplane of the disk, consistent with optically thick emission, almost certainly from dust (Plambeck & Wright 2016). The spectral index steepens to ~ 3 at the edges and ends of the disk, indicating emission from optically thin dust. In Figure 2, we see that the central source is more prominent at 43 GHz, and also note the steepening of the spectral index at the ends of the disk between 43 and 99 GHz.

Uncertainties in the spectral indices are dominated by the absolute flux calibration accuracy of $\sim 10\%$ for each frequency band. A multiplicative error in the flux ratio is an additive error in the spectral index of $+0.15$ and -0.18 in the 340/99 GHz

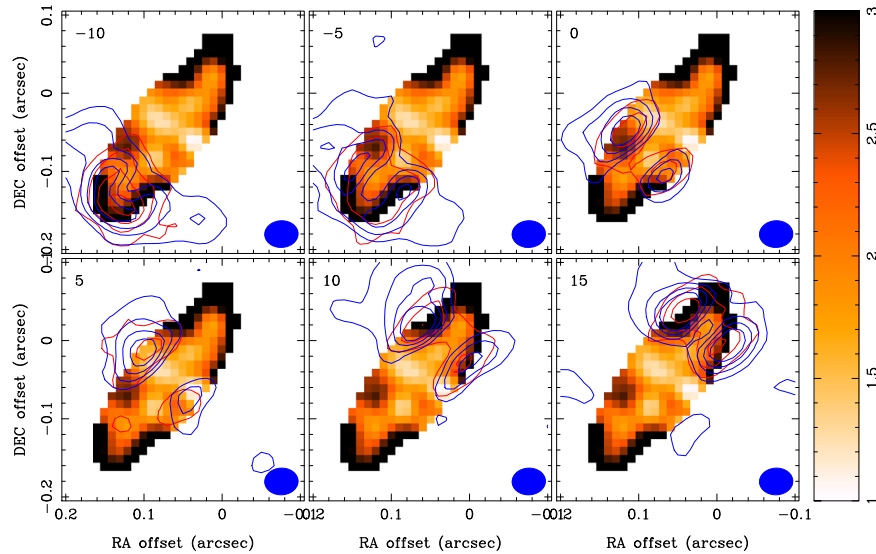


Figure 7. Comparison of NaCl emission at 232.51 GHz and 335.51 GHz averaged in 5 km s^{-1} channels, overlaid on the spectral index image. The red contours in the NaCl line at 232.51 GHz show the contour interval of 20 K. The blue contours in the NaCl line at 335 GHz show the contour interval of 20 K. The channel at 15 km s^{-1} is only 4.3 km s^{-1} wide to avoid contamination from adjacent spectral lines. The 30×40 mas convolving beam FWHM is indicated in blue in the lower right.

spectral index image, $+0.22$ and -0.28 in the 223/99 GHz image, and $+0.11$ and -0.13 in the 99/43 GHz image. A least-squares fit from 43–340 GHz to the spectral index at the central position gives 1.6 ± 0.1 , whereas at the ends of the disk the fitted spectral index is 3.4 ± 0.3 . The spectral index variations across the images are significant.

3.2. Disk Structure

Ginsburg et al. (2018) fitted the observed structure of the disk from B3 and B6 ALMA continuum observations at 50 and 20 mas resolution, respectively. They determined that the disk has a length of ~ 100 au and a vertical FWHM height of ~ 20 au. They also detected a compact source near the center of the disk, smeared parallel to the disk major axis. The model residuals shown by Ginsburg et al. (2018) have a halo of emission at the ~ 30 K level in the B6 image that may be from optically thin dust, as it was not seen in the B3 image. This halo of emission is evident in Figure 3, where both B3 and B6 are plotted at the same logarithmic contour levels.

Table 2 summarizes the results of Gaussian fits to the disk size in our four continuum images. The disk major axis increases with observing frequency, which is expected as the dust optical depth increases. The minor axis is largest at 43 GHz, however, indicating that the central point source is more prominent at lower frequencies.

If we assume that the disk is circular and infinitesimally thin, we can set a lower limit on its inclination angle. The 224 and 340 GHz source sizes given in Table 2 imply that this lower limit is 78° – 80° .

In Figure 4 we show a maximum entropy image of the B7 continuum emission. The lower limit to the inclination estimated from the major and minor axes of the maximum entropy image is $79^\circ \pm 1^\circ$ measured at the 400 K contour (99×19 au), and $74^\circ \pm 1^\circ$ measured at the 25 K contour (239×45 au). The lowest contours at the ends of the disk suggest a flared structure, so the inclination measured at the 400 K contour is better determined. If the disk were inclined by as much as 74° or 79° , the ~ 20 au disk thickness, would imply that the southwest edge should be slightly curved. The incredibly straight southwest edge in Figure 4 suggests that the inclination is closer to 90° .

A third estimate of the disk orientation can be obtained from the SiO outflow. At the highest velocities, the SiO outflow is blueshifted to the northeast, and redshifted to the southwest. This is more easily seen in Figure 1 of Plambeck et al. (2009), which maps the large-scale structure of the SiO outflow. The blueshifted emission at -13.5 km s^{-1} subtends an angle of 27° at a radius ~ 1300 au to the northeast, and the redshifted emission at 21.9 km s^{-1} subtends an angle of 26° at a radius of ~ 1400 au. The red–blue asymmetry in the outflow implies that the northeast edge of the disk faces toward us. Proper motion measurements of compact structures in the outflow could enable us to derive an inclination from the SiO outflow. Matthews et al. (2010) derived an inclination $\sim 85^\circ$ from SiO masers close to the disk.

In Figure 5, we compare maximum entropy images of the 340 and 223 GHz continuum emission, both convolved by a 10 mas Gaussian beam. As expected, the convolution reduces the gradients at the edges of the disk, which are still steeper on the northeast edge than the southwest edge. In both images, the brightness temperature plateau of the disk, ignoring the compact source on the northeast side, is ~ 400 K. The brightness falls to ~ 200 K on the 223 GHz image, where the brightness on the 340 GHz image is still ~ 400 K. If we attribute this to dust emission, then the dust opacity at 223 GHz is ~ 0.7 , where the emission is still optically thick at 340 GHz. At the disk edges, the logarithmic contour levels are approximately evenly spaced, suggesting an exponential gradient in the emission. The $1/e$ scale height estimated from the gradient between 400 and 25 K at the edge of the disk at 340 GHz ~ 2 au on the facing, northeast side, to ~ 4 au on the SW side. We may be seeing deeper into the disk on the facing, northeast side where the continuum emission is brighter.

Since the disk surface layers are being torn up by the outflow as the dust grains are destroyed, however, it is likely that the spectral index of the dust emission varies through the surface layers, and we do not further interpret the density profile of the disk surface.

3.3. Salt Emission

Figure 6 shows NaCl emission at 232.51 GHz overlaid on contours of 99 and 340 GHz continuum images. Salt emission is found in the dust layer at the surface of SrcI where there is a large

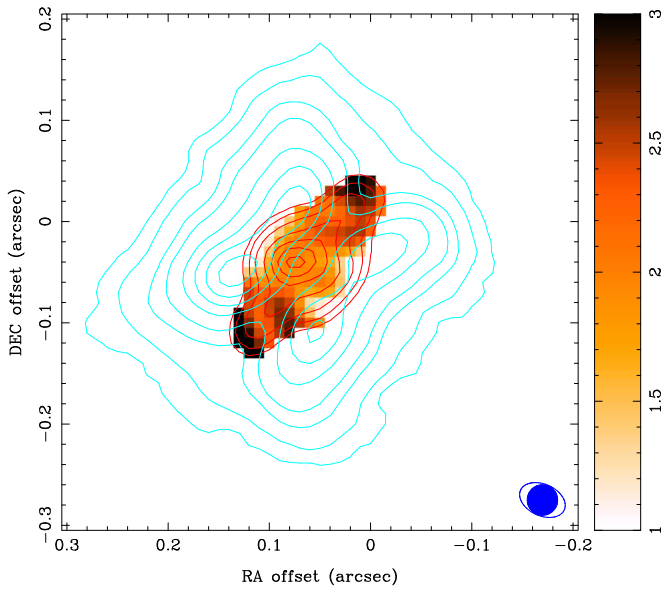


Figure 8. H₂O emission at 232.687 GHz. The color image shows the 43–99 GHz spectral index. The red contours show the 43 GHz continuum emission at levels: 50, 100, 200, 400, 600, 800, 1000, 1200, and 1400 K. The blue contours show the H₂O emission at 232.6867 GHz integrated over a velocity range of (–50 to 50) km s^{–1}. The contour levels are 0.05, 0.1, 0.2, 0.3, 0.5, 0.7, 0.9, and 1.1 × 15,345 K km s^{–1}. The 30 mas convolving beam FWHM for the continuum image and spectral index image is indicated in the blue filled circle. The FWHM beam for the H₂O emission was 0.05 × 0″.03 in PA 65°, shown as the open ellipse in the lower right.

spectral index gradient. A gradient in the dust opacity may help to explain the discrepancy in the NaCl excitation temperatures estimated from rotationally and vibrationally excited levels (Ginsburg et al. 2019). Figure 7 shows a comparison of NaCl emission at 232.51 and 335.51 GHz averaged in 5 km s^{–1} channels, overlaid on the spectral index image between 99 and 223 GHz. Both NaCl lines have peaks in the surface layers on both sides of the disk at close to the same positions. The 335 GHz NaCl $\nu = 1, J = 26 - 25$ line is strongly attenuated where the spectral index is less than ~ 2 . The 232 GHz NaCl $\nu = 1, J = 18 - 17$ line is less attenuated and shows a bridge of emission between the two peaks. The NaCl emission is brighter on the northeast side of the disk which is facing toward us. This could also be because there is less attenuation by the disk. Thus, we suggest that the rotational temperatures, over a large range of observing frequencies, could be underestimated because of greater dust opacity at high frequencies, whereas the vibrational temperatures, over a small range of frequencies, are less affected.

4. The SrcI Outflow

4.1. H₂O

Figure 8 shows H₂O emission at 232.687 GHz overlaid on the 43 GHz continuum and spectral index images. H₂O emission extends from the surface of the SrcI disk into the outflow, and rotates with the SrcI disk. In contrast with the salt emission, the H₂O emission is more closely associated with the inner part of the disk, shown here at 43 GHz. The H₂O emission may be, in part, excited by radiation from the central source, and is brighter on the northeast side where we see deeper into the disk. Hirota et al. (2017) present a model where the H₂O comes from the disk surface, and is driven by a magnetocentrifugal disk wind (Matthews et al. 2010; Greenhill et al. 2013; Vaidya & Goddi 2013; Hirota et al. 2017).

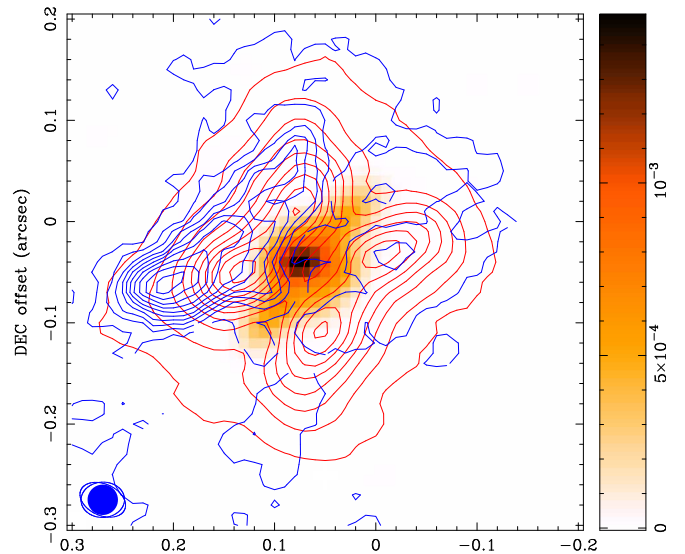


Figure 9. AIO $N = 6 - 5$ emission at 229.6938725 GHz overlaid on the 43 GHz continuum, and H₂O emission at 232.6867 GHz. The red contours show the H₂O emission at 232.6867 GHz integrated over a velocity range of (–50 to 50) km s^{–1}. The lowest contour is 933, and the contour interval is 1866 K km s^{–1}. The blue contours show the AIO $N = 6 - 5$ emission integrated over –50 to 50 km s^{–1}. The lowest contour is 225, and the contour interval is 450 K km s^{–1}. The 30 mas convolving beam FWHM for the 43 GHz continuum image is indicated in as the blue filled circle. The FWHM beams for the H₂O emission of 0.05 × 0″.03 in PA 65°, and for the AIO $N = 6 - 5$, 0.04 × 0″.03 in PA –88°, are shown as the open ellipses in the lower left.

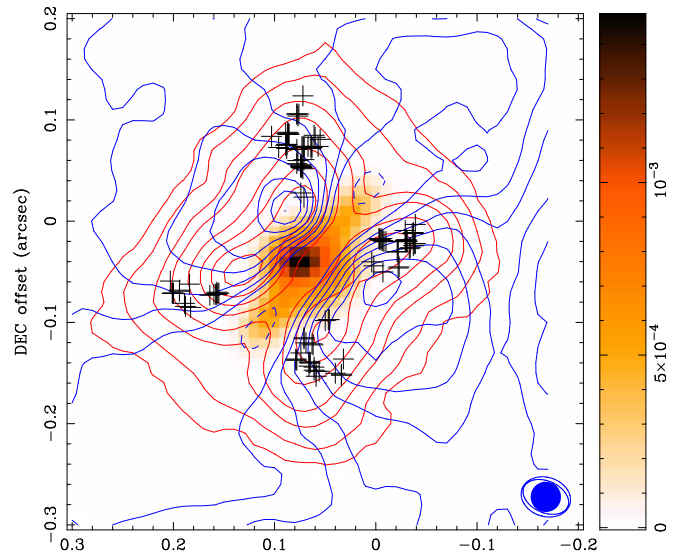


Figure 10. SiO $\nu = 0 J = 5 - 4$ emission at 217.10498 GHz overlaid on the 43 GHz continuum and H₂O emission at 232.6867 GHz. The color image shows the 43 GHz continuum emission. The red contours show the H₂O emission at 232.6867 GHz integrated over a velocity range of –50 to 50 km s^{–1}. The contour levels are 0.05, 0.1, 0.2, 0.3, 0.5, 0.7, 0.9, and 1.1 × 15,345 K km s^{–1}. The blue contours show the SiO $\nu = 0, J = 5 - 4$ emission integrated over the spectral line. The contour interval is 2589 K km s^{–1}. The 30 mas convolving beam FWHM for the 43 GHz continuum image is indicated as a blue filled circle. The FWHM beams for the H₂O emission of 0.05 × 0″.03 in PA 65°, and for the SiO $\nu = 0, J = 5 - 4$, 0.05 × 0″.04 in PA 73°, are shown as the open ellipses in the lower right. The black crosses indicate the centroid positions of the $\nu = 1, J = 2 - 1$ SiO masers mapped by Issaoun et al. (2017).

4.2. AIO

We mapped the AIO $N = 6 - 5$ line at 229.69387 GHz, and the AIO $N = 9 - 8$ line at 344.4537 GHz. Figure 9 shows the 229.694 GHz AIO emission overlaid on the 43 GHz continuum

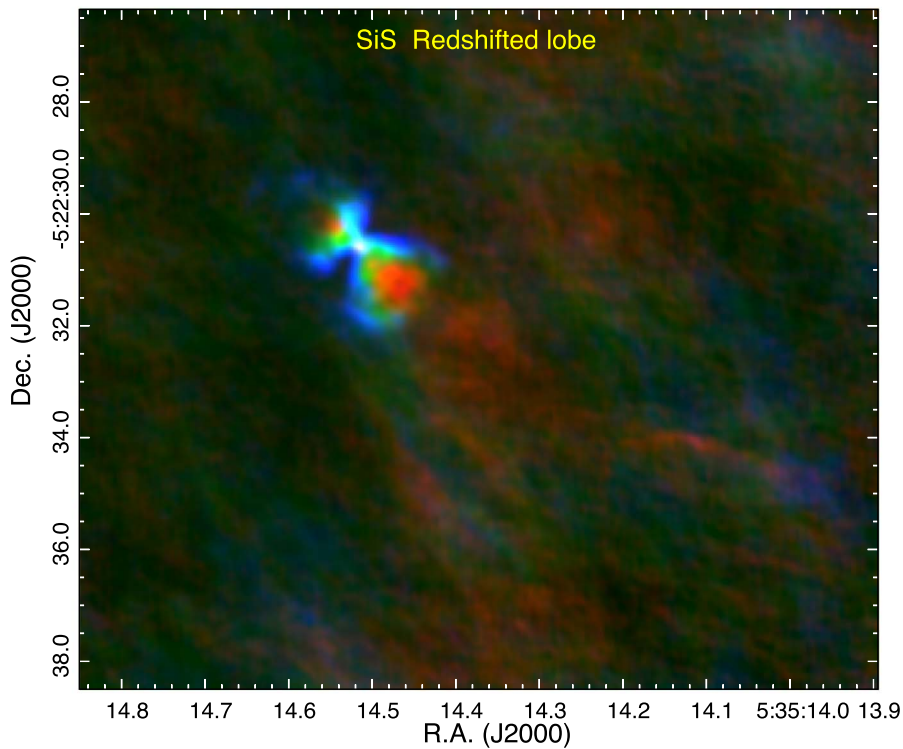


Figure 11. Three-color image of SiS (217.81766 GHz) emission. Blue +4 to +8 km s⁻¹, Green +9 to +16 km s⁻¹, Red +17 to +30 km s⁻¹. The velocity ranges are chosen to highlight the enhancement of SiS emission around the SrcI outflow in the redshifted lobe.

and H₂O emission at 232.687 GHz. The AIO emission is coextensive with H₂O, but the peaks are farther out, and brighter on the northeast side of SrcI. Since the northeast side of the disk is facing toward us, we may be able to see deeper into the central regions. The distributions of AIO emission and H₂O shown here are consistent with those presented by Tachibana et al. (2019) for AIO $N = 13 - 12$ and $N = 17 - 16$ emission lines at 497 and 650 GHz, and H₂O at 643 GHz (Hirota et al. 2017). Tachibana et al. (2019) attribute the distribution of AIO as due to its formation at the base of the outflow, and condensation further out into the outflow. Our observations with $\sim 4\times$ higher angular resolution suggest that AIO emission peaks downstream of the H₂O, and may be produced by grain destruction and oxidized by O released by the dissociation of H₂O, or released as AIO further out in the outflow than the H₂O emission.

4.3. SiO

The SiO masers associated with SrcI have been mapped using very long baseline interferometry at 43 GHz (Kim et al. 2008; Matthews et al. 2010), and 86 GHz (Issaoun et al. 2017). The $J = 1 - 0$ and $J = 2 - 1$, $\nu = 1$ and $\nu = 2$ maser positions lie in an X pattern, with blueshifted emission in the south and east arms, and redshifted emission in the north and west arms. The $J = 1 - 0$ and $J = 2 - 1$ $\nu = 1$ and $\nu = 2$ masers can be interpreted as tracing a wide-angle outflow arising from the surface of the almost edge-on rotating disk (Issaoun et al. 2017). No masers are located within a 14 au band in PA $\sim 141^\circ$ that corresponds to the continuum emission from the disk (Matthews et al. 2010). Goddi et al. (2009) modeled the SiO maser excitation including both radiative and collisional excitation. The model predicts densities $n_{\text{H}_2} = 10^8 - 10^{10} \text{ cm}^{-3}$ for the $\nu = 1$, and $10^9 - 10^{11} \text{ cm}^{-3}$ for the $\nu = 2$ transitions. The $\nu = 2$ transition is favored where $T_k > 2000 \text{ K}$, closer to SrcI

than $\nu = 1$ as is observed (Kim et al. 2008; Matthews et al. 2010). Figure 10 shows SiO $\nu = 0$, $J = 5 - 4$ emission at 217.10498 GHz overlaid on the 43 GHz continuum and 232.69 GHz H₂O emission. The centroid positions of the $J = 2 - 1$ masers mapped using the Very Long Baseline Array are indicated by the black crosses that lie along the ridges of the peak H₂O emission. H₂O peaks closer to the disk, and SiO extends farther into the lobes. The SiO $\nu = 0$, $J = 5 - 4$ distribution is similar to that of the SiO $\nu = 2$, $J = 10 - 9$ mapped by Kim et al. (2019). Kim et al. (2019) also mapped the $^{29}\text{SiO } \nu = 2$ $J = 11 - 10$ and SiO $\nu = 4$ $J = 11 - 10$ lines. The spatial and velocity distribution of these high excitation lines also suggest that they are associated with the base of the outflow at the surface of the disk.

These distributions fit into a scenario where the SiO is formed from grain destruction following the dissociation of H₂O (Schilke et al. 1997). In these models, grain mantles and grain cores are destroyed in shocks; Si is released into the gas phase, and then oxidized by dissociation products of H₂O. In the SrcI disk Si can be ablated from disrupted grains by shock velocities $> 25 \text{ km s}^{-1}$. In the postshock gas, H₂O is depleted onto grains and converted to OH. OH reacts with Si to form SiO, and SiO₂ if OH is abundant. Cohen et al. (2006) note the absence of OH masers within 1300 au of SrcI where SiO is prominent. OH masers occur in densities $n_{\text{H}_2} \sim 10^7 \text{ cm}^{-3}$, close to a shock front where the OH abundance is high. Gain path lengths 1–10 au, not necessarily contiguous, suffice to produce OH masers (Gray et al. 1992), so either chemistry or maser excitation is responsible for their absence closer to SrcI. Greenhill et al. (2013) suggest that shocks from a magnetocentrifugal wind from SrcI, can inject energy further out in the outflow where the outflow speed exceeds the Alfvén and sound speeds. SiO emission extends from the surface of SrcI into the extended outflow lobes, and rotates with SrcI. SiO is a good

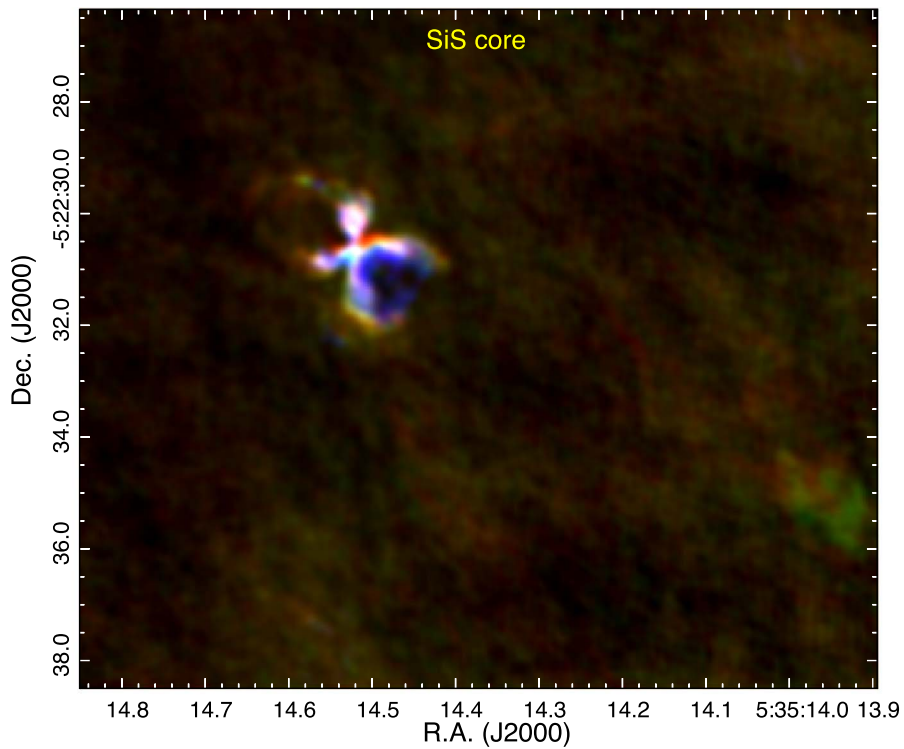


Figure 12. Three-color image of SiS (217.81766 GHz) emission. Blue -3 to -1 km s^{-1} , Green 0 km s^{-1} , Red $+1$ to $+3$ km s^{-1} . The velocity ranges are chosen to highlight the enhancement of SiS emission around the SrcI outflow in the SiS core.

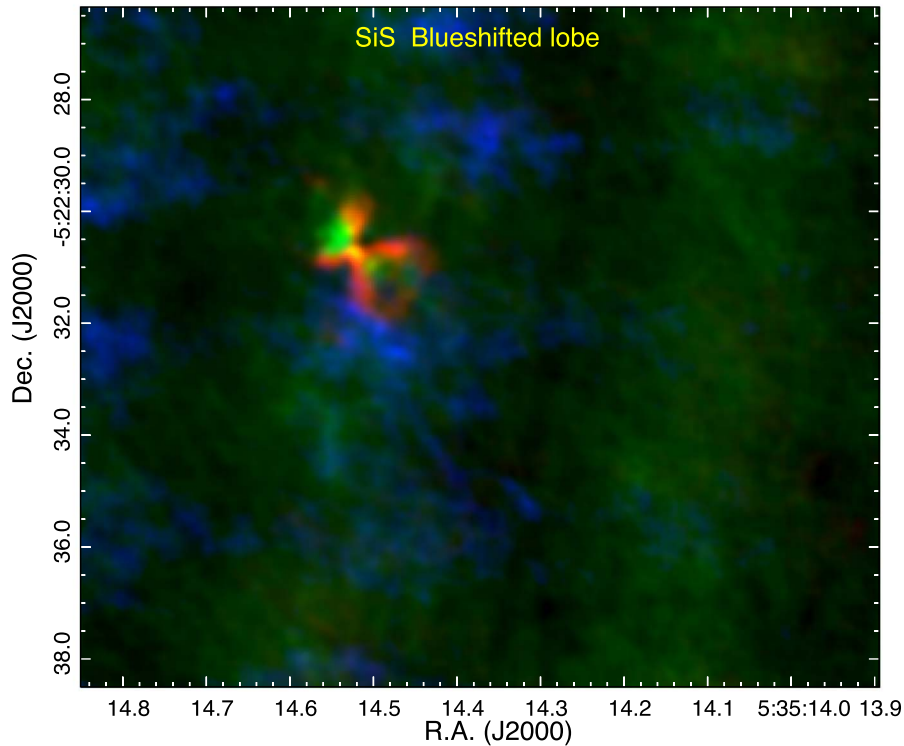


Figure 13. Three-color image of SiS (217.81766 GHz) emission. Blue -23 to -12 km s^{-1} , Green -11 to -7 km s^{-1} , Red -6 to -3 km s^{-1} . The velocity ranges are chosen to highlight the enhancement of SiS emission around the SrcI outflow in the blueshifted lobe.

tracer of shocks. The implication is that the OH is depleted in the inner regions where there is free Si. Our data suggest that chemistry and shock excitation play a significant role in determining these molecular distributions.

4.4. SiS

Figures 11–13 show three-color images of the 217.817 GHz SiS line. These color images clearly show the wide-angle bipolar wind from SrcI. This feature in SiS is highly

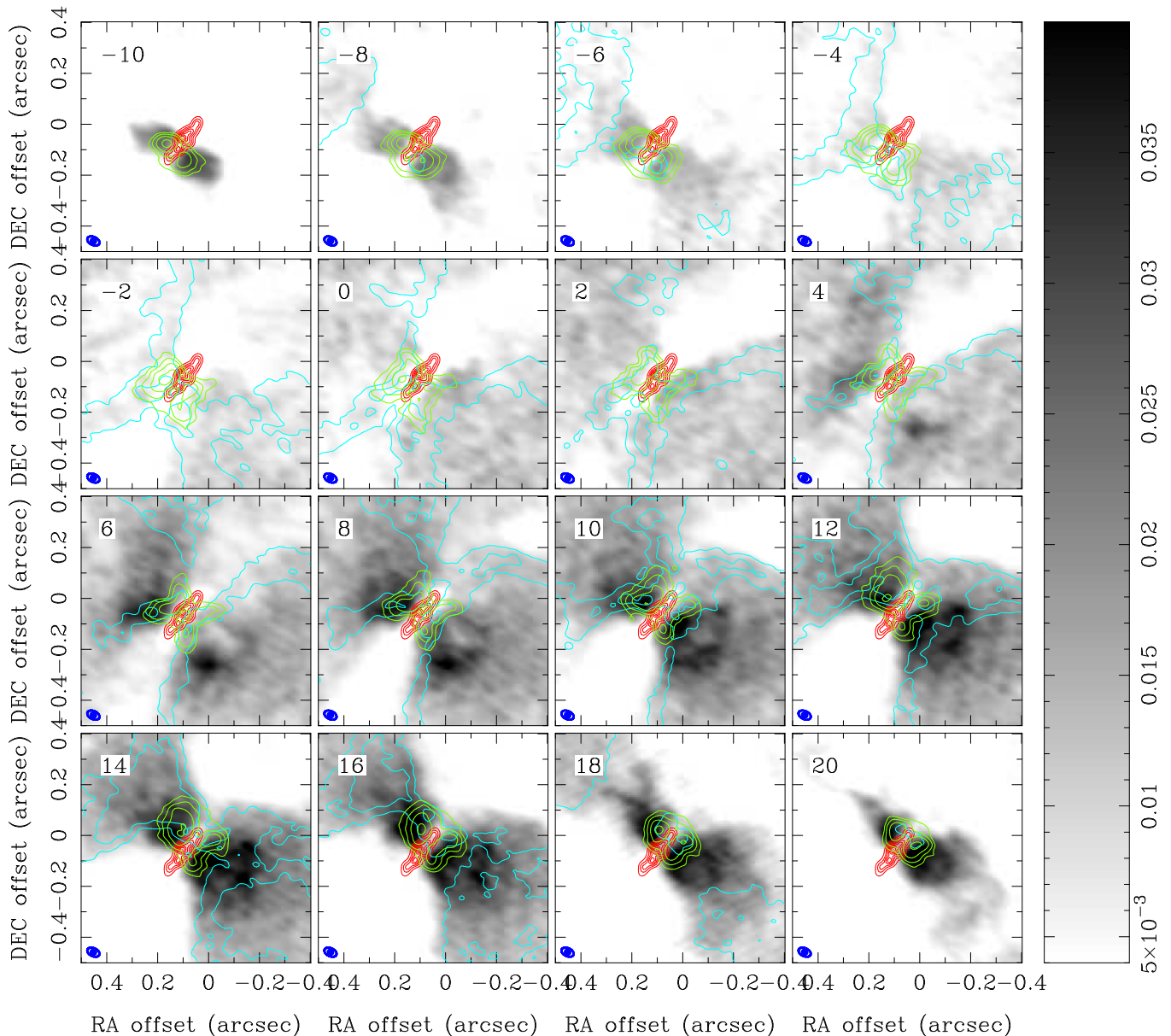


Figure 14. Grayscale shows SiO (217.10498 GHz) in 2 km s^{-1} channels and ranges from 4–40 mJy beam^{-1} . The red contours show the 99 GHz continuum with contour levels of 1, 2, 3, 4, 5, 6, 7, and 8 mJy beam^{-1} in a 30 mas beam. The blue contours show SiS (217.81766 GHz) in 2 km s^{-1} channels, with contour levels at 100, 200, and 400 K in a 50×30 mas beam. The green contours show H_2O (232.6867 GHz) in 2 km s^{-1} channels, with contour levels at 100, 200, and 400 K in a 50×30 mas beam. The convolving beams is indicated in blue in the lower left.

limb-brightened. In addition to motion away from SrcI with the blueshifted lobe extending northeast and the redshifted lobe extending southwest, the SiS outflow exhibits rapid expansion away from the outflow axis. The SiS outflow is highly asymmetric with a stubby northeast blue lobe and a much longer southwest red lobe. Weak emission can be traced to the lower right edge of the figures above. Also note the patch of SiS emission near the southwest corner of the image at the “core” velocities.

Figure 14 compares the 217.817 GHz SiS line with the SiO and H_2O emission in 2 km s^{-1} velocity channels. Like SiO and H_2O , SiS shows rotation close to SrcI. Approximately 50 au above and below the SrcI disk, close to the maximum extent of the H_2O emission region, the SiO column expands abruptly into a turbulent wide-angle outflow. Filaments of SiS emission are particularly prominent along the edges of the outflow.

The distributions of SiO and SiS are consistent with the model of Podio et al. (2017), who argue that SiO results from dust grain destruction, whereas SiS is the product of gas-phase chemistry. SiO and SiS are also seen in L1157-B1 in the outflow from this low-mass protostar (Podio et al. 2017). As in Orion, SiO and SiS have different spatial distributions: SiO is seen where the molecular jet impacts the outflow cavity wall, but SiS is detected only at the leading edge of the outflow. Zanchet et al. (2018) also considered silicon, oxygen, and sulfur chemistry in postshock gas in protostellar outflows. They found that the main SiS-forming reactions are $\text{Si} + \text{SO}$ and $\text{Si} + \text{SO}_2$, and that SiS is efficiently destroyed through reaction with atomic oxygen.

4.5. SO and SO_2

Figure 15 shows the SO emission at 344.31 GHz, and SO_2 at 334.67 GHz in 2 km s^{-1} velocity channels. Both SO and SO_2

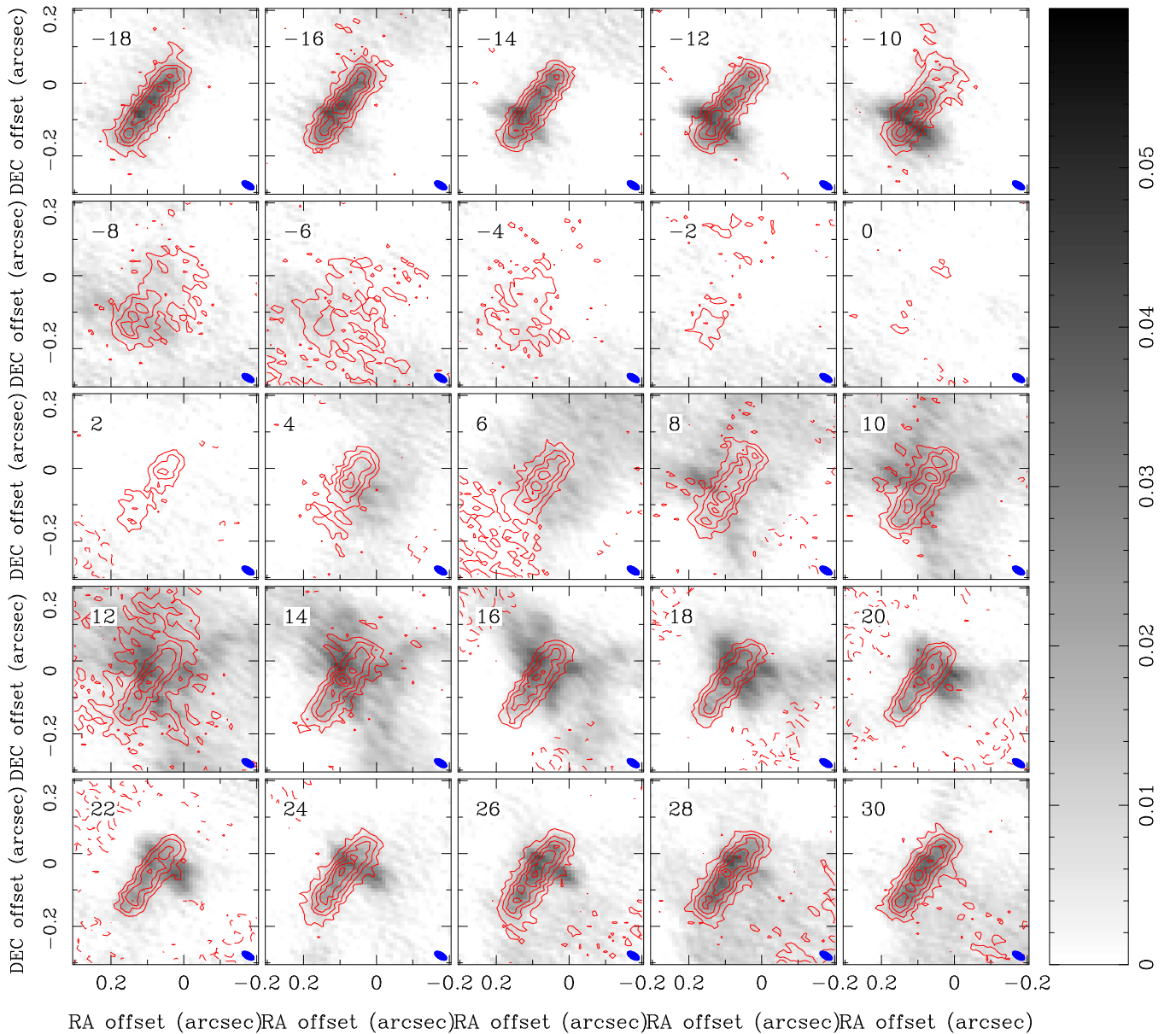


Figure 15. SO and SO₂ emission and absorption across SrcI. Both images plot line emission + continuum emission from the disk to show the line absorption across the disk. The grayscale image shows the SO at 344.31 GHz. The peak 0.039 Jy/beam = 655 K. The contours show the SO₂ at 334.67 GHz. The contour interval is 129 K, and the peak is 729 K. The convolving beam 36×17 mas FWHM in PA = 59 deg is indicated in blue in the lower right.

are heavily absorbed across SrcI at velocities of -8 to $+4$ km s⁻¹. This is consistent with the $0''.2$ resolution spectra of SrcI plotted by Plambeck & Wright (2016), in which sulfur-bearing species, including CS and H₂S as well as SO and SO₂, exhibit prominent blueshifted absorption profiles. Since the velocity width of the absorption is comparable with the halfwidth of the SiO emission lines, it is likely that the absorbing molecules are located in the (cooler) outer layers of the SrcI outflow, rather than in unrelated foreground gas. Examining Figure 15, one sees that SO emission (grayscale) follows the rotation of the outflow close to the disk, while SO₂ does not show this small scale structure. Models of C-type shocks with velocities of $5\text{--}40$ km s⁻¹ and densities of $10^4\text{--}10^6$ cm⁻³ can enhance SO and SO₂ abundances by two orders of magnitude. SO decreases quickly after the passage of a shock, while SO₂ is enhanced during, and for some time after, the shock (Pineau des Forets et al. 1993).

The SO and SO₂ distributions are over-resolved in these ALMA observations. At lower resolution, SO and SO₂ are seen as a shell of expanding gas, with enhanced abundances where the outflow from SrcI impacts dense clumps around the edges of the outflow (Wright et al. 1996; Wright & Plambeck 2017). Goddi et al. (2011a) suggested that the hot core is excited by the SrcI outflow impacting a dense core. The correspondence of these continuum clumps with the edge of the outflow is shown in Figure 16.

4.6. Unidentified Line Emission along the Outflow Axis

Figure 16 also shows an unidentified line that appears in two lobes along the outflow axis, centered on SrcI. Assuming the line is centered at 5 km s⁻¹, like the SiO, the rest frequency of the U-line is 354.4945 GHz. Gaussian fits to the spectra at the two peaks give velocities of 4.3 ± 0.1 , FWHM 5.8 ± 0.2 km s⁻¹ for

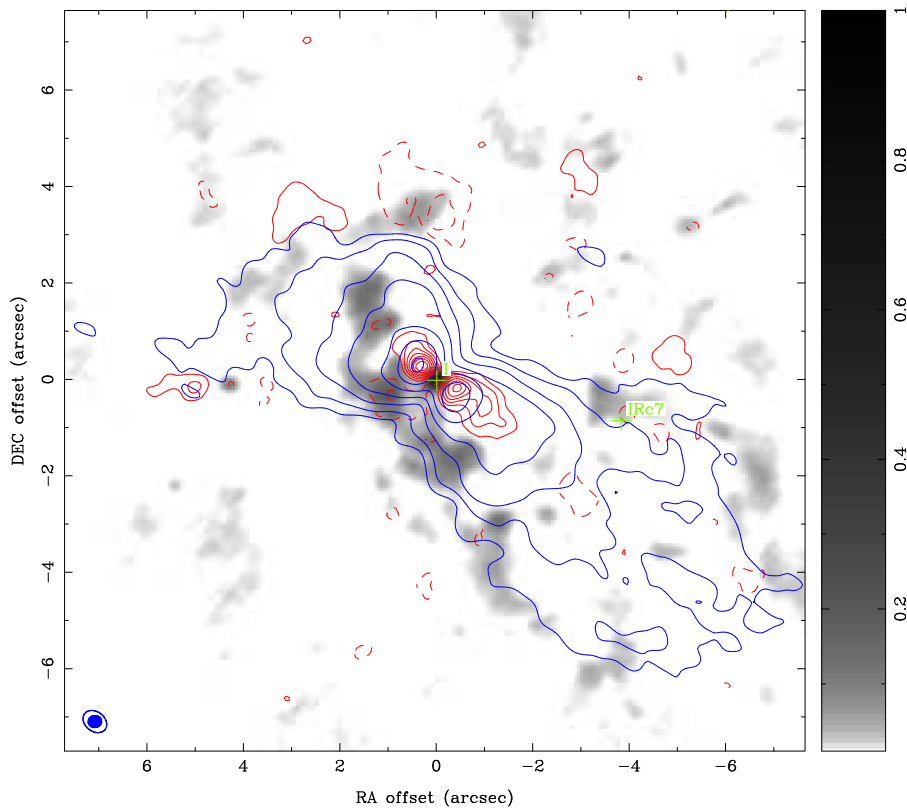


Figure 16. Continuum emission around the edges of the SiO $J = 2 - 1 \nu = 0$ line (blue contour levels of 0.05, 0.1, 0.2, 0.4, 0.8, 1.6, and 3.2 Jy/beam (746 K Jy^{-1}), integrated over -10 to $+20 \text{ km s}^{-1}$). The red contours map the integrated emission over 11 km s^{-1} from an unidentified line at 354.4945 GHz (141 K Jy^{-1}). The contour interval is 14.8 K . The grayscale image shows the continuum emission at 348 GHz (141 K Jy^{-1}). The convolving beams, $0.28 \times 0''.26$ for the unidentified line and continuum emission and $0.54 \times 0''.41$ for the SiO, are indicated in blue in the lower left.

the northeast peak, and $+5.7 \pm 0.1 \text{ km s}^{-1}$, FWHM $6.7 \pm 0.2 \text{ km s}^{-1}$ for the southwest peak.

The U-line is blueshifted to the northeast like the SiO outflow, but the FWHM is smaller, and the emission is more confined along the outflow axis. There is a vibrationally excited HCN line at 354.4604 GHz $\sim 26 \text{ km s}^{-1}$ from the U-line centered on 354.4945 GHz in this image. The U-line image has well-defined spectral peaks, and has low sidelobes and is probably therefore quite compact, whereas the image of the HCN line emission has large sidelobes suggesting missing larger-scale structure. The U-line could be an SiO isotopologue or a high vibrational transition illuminated by the central source. The Lovas catalog lists an unidentified line at 354.4968 GHz . In the Cologne Database for Molecular Spectroscopy catalog there are many lines from 354.49 to 354.50 GHz . Most of them are organic molecules except TiO_2 at 354.4977 GHz , but it is also not convincing.

5. Discussion and Conclusions

Our analysis has focused on understanding whether the chemistry seen in SrcI is a result of an “anomalous” history of interactions with its environment, or whether it is directly attributable to the physical conditions of SrcI and its associated outflow, making SrcI a paradigm for the study of high-mass star formation.

The distributions of H_2O , SiO, AlO, and SiS lend strong support to a model in which dust grains are ablated and destroyed close to the disk surface, producing an oxygen-rich outflow. The strong SiO maser emission, and AlO mapped in the outflow close to the disk, suggest that refractory grain cores as

well as the grain mantles are destroyed. Lenzuni et al. (1995) investigated the evaporation of dust grains in protostellar cores. Carbon grains are destroyed at temperatures of $\sim 800\text{--}1150 \text{ K}$. Silicate grains are evaporated at temperatures of $\sim 1300 \text{ K}$, followed by AlO at $\sim 1700 \text{ K}$. SiO and AlO may be released directly from the grains, or may be formed in the gas phase by the oxidation of Si and Al. Thermal emission of SiO from the ground state, $\nu = 0$, traces a turbulent, wide-angle outflow extending over 1000 au from a position close to the maximum extent of the H_2O emission from the disk (Plambeck et al. 2009). SiS traces a more filamentary structure which is prominent at the edges of extended SiO outflow. Zanchet et al. (2018), in a study of silicon, oxygen, and sulfur chemistry, found that the main formations for SiS are from SO and SO_2 which are seen as a shell around the edges of the outflow (Wright et al. 1996).

One might ask if the chemistry of the bipolar outflow is distinct from that of the larger “finger system” produced by the BN–SrcI explosive event. The finger system is over an arcminute in extent, and so is almost completely resolved out in our high-resolution images. CO emission from the fingers was mapped by Bally et al. (2017) with an approximately $1''$ resolution using mosaicked observations with ALMA. Those data also cover transitions of SiO ($J = 5 - 4 \nu = 0$; 217.105 GHz), SO (219.95 GHz), and SO_2 (216.64 GHz). We used the mosaicked ALMA data to generate 2 km s^{-1} channel maps of these three molecular lines over a $30''$ region centered on SrcI. These images are compared in Figure 17. Both the SiO and SO images exhibit streamers similar those seen in CO; the situation for SO_2 is less clear. The SiO fingers east of SrcI at velocities $>30 \text{ km s}^{-1}$ were noted earlier by Plambeck et al. (2009; see their Figure 4). It is

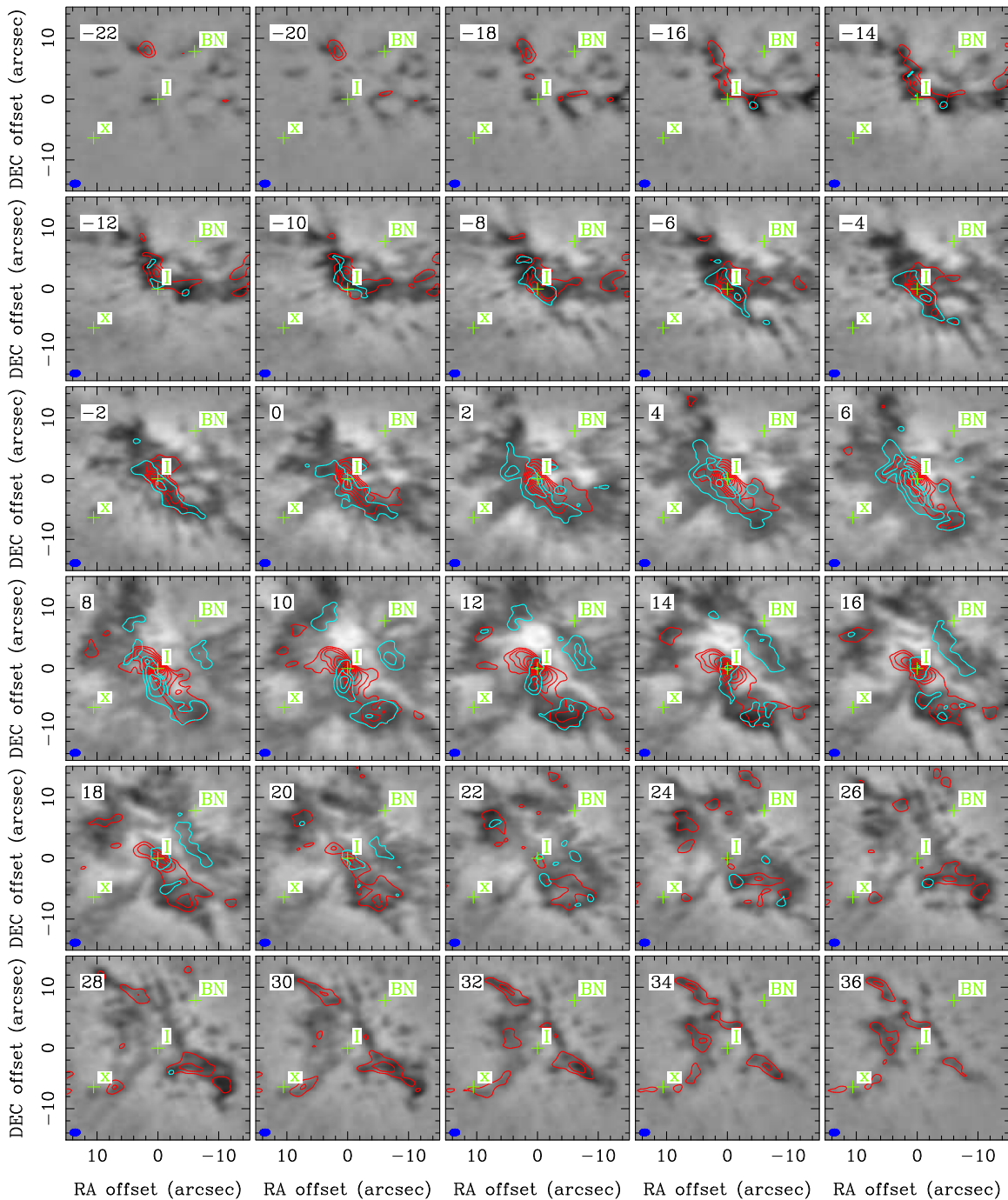


Figure 17. SiO, SO, and SO₂ emission associated with the explosion resulting from the SrcI/BN interaction. The grayscale image shows the SO at 219.95 GHz. The extended SO emission is heavily resolved in these ALMA observations, but nicely shows the filamentary structure. The red contours show the SiO emission at 217.10 GHz, and the blue contours show the SO₂ emission at 216.64 GHz. The contour interval is 19 K in both SiO and SO₂. The convolving beam FWHM of $1''.5 \times 0''.9$ is indicated in blue in the lower left.

extremely difficult to distinguish the outflow from the finger system in any of these images. In these molecular lines, at least, there appear to be no clear chemical or excitation differences between the bipolar outflow and the explosive event.

It is possible that the SrcI/BN interaction, resulting in a collapse of a binary protostar in SrcI and the disruption of the disk around SrcI, dredged up the inner part of the disk and made oxygen- and sulfur-rich material available for both the SrcI outflow and the explosion. It may also have moved dust grains containing refractory material like AlO and salts to the

outer parts of the disk where they could be ablated by the SrcI outflow. The energy for the ejection of SrcI and BN, and the explosion in the gas, must have come from gravitational binding energy exceeding 10^{48} erg (Bally et al. 2017). The violence of the interaction ~ 550 yr ago would have strongly shocked the disk, resulting in chemistry. The AlO and salts could be a byproduct of this interaction. As the disk relaxed from its perturbed state, it could have triggered a major accretion event onto the central binary or a merger which produced the current SrcI outflow of about the same age. At

50 au, the disk is well inside the SrcI gravitational radius for a 10 km s^{-1} ejection speed. Thus, the disk is likely made of material that was already bound to one or more of the stars involved in the interaction—no need for Bondi–Hoyle accretion over the last 500 yr. Moeckel & Goddi (2012) studied the chances of disk survival in binary–single stellar interactions with N -body simulations.

Observations of other high-mass protostar outflows are required to see if H_2O , sulfur, and Si molecules, and salts are common or if the SrcI outflow is unusual. We adopt as a working hypothesis that the rich chemistry seen in SrcI is a direct consequence of the outflow from a high-mass protostar and does not depend on the particular environment and history of SrcI.

If Orion SrcI, as the closest and best studied example of a young high-mass protostar, is indeed a paradigm model, then future observations of other high-mass star formation regions will have many tools available. The resolution and sensitivity of our ALMA observations are sufficient to detect disks and outflows similar to those seen in SrcI out to ~ 2 kpc. Our ~ 50 mas resolution images (100 au at 2 kpc) have an rms brightness sensitivity of ~ 10 K at 2 km s^{-1} velocity resolution, which would be sufficient to detect and image SiO, SiS, H_2O , and salt distributions in outflows from putative disks around other high-mass protostars.

Our observations from 43–350 GHz allow us to map the dust opacity at the surface of the disk around SrcI. NaCl and KCl trace the rotation of the surface layers of SrcI, allowing us to estimate the mass of the protostar. Salt emission is confined to the dust layer where there is a large spectral index gradient. NaCl excitation temperatures estimated from rotational transitions over a large range of frequencies could be underestimated because of greater dust opacity at high frequencies, whereas the vibrational temperatures, estimated over a small range of frequencies, are less affected.

H_2O emission maps the distribution of material released from grain mantles. SiO maps the more extended outflow. Maps of SiS and SO in other outflows could support the role of gas-phase chemistry in the postshock gas in the outflow.

This paper makes use of the following ALMA data: ADS/JAO.ALMA#2012.1.00123.S, ADS/JAO.ALMA#2013.1.00546.S, ADS/JAO.ALMA#2016.1.00165.S, and ADS/JAO.ALMA#217.1.00497.S. ALMA is a partnership of ESO (representing its member states), NSF (USA) and NINS (Japan), together with NRC (Canada) and MOST and ASIAA (Taiwan), and KASI (Republic of Korea), in cooperation with the Republic of Chile. The Joint ALMA Observatory is operated by ESO, AUI/NRAO and NAOJ.

The National Radio Astronomy Observatory is a facility of the National Science Foundation operated under cooperative agreement by Associated Universities, Inc. T.H. is financially supported by the MEXT/JSPS KAKENHI grant Nos. 24684011, 17K05398

and 18H05222. We thank the referee, Paul Ho, for a careful reading which has improved the presentation of this paper.

Facilities: ALMA, VLA.

Software: Miriad (Sault et al. 1995).

ORCID iDs

Melvyn Wright  <https://orcid.org/0000-0002-9154-2440>
 Richard Plambeck  <https://orcid.org/0000-0001-6765-9609>
 Tomoya Hirota  <https://orcid.org/0000-0003-1659-095X>
 Adam Ginsburg  <https://orcid.org/0000-0001-6431-9633>
 Brett McGuire  <https://orcid.org/0000-0003-1254-4817>
 John Bally  <https://orcid.org/0000-0001-8135-6612>

References

- Bally, J., Ginsburg, A., Arce, H., et al. 2017, *ApJ*, **837**, 60
 Cohen, R. J., Gasprong, N., Meaburn, J., & Graham, M. F. 2006, *MNRAS*, **367**, 541
 Ginsburg, A., Bally, J., Goddi, C., Plambeck, R., & Wright, M. 2018, *ApJ*, **860**, 119
 Ginsburg, A., McGuire, B., Plambeck, R., et al. 2019, *ApJ*, **872**, 54
 Goddi, C., Greenhill, L. J., Chandler, C. J., et al. 2009, *ApJ*, **698**, 1165
 Goddi, C., Greenhill, L. J., Humphreys, E. M. L., Chandler, C. J., & Matthews, L. D. 2011a, *ApJL*, **739**, L13
 Goddi, C., Humphreys, E. M. L., Greenhill, L. J., Chandler, C. J., & Matthews, L. D. 2011b, *ApJ*, **728**, 15
 Gómez, L., Rodríguez, L. F., Loinard, L., et al. 2008, *ApJ*, **685**, 333
 Gray, M. D., Field, D., & Doel, R. C. 1992, *A&A*, **262**, 555
 Greenhill, L. J., Goddi, C., Chandler, C. J., Matthews, L. D., & Humphreys, E. M. L. 2013, *ApJL*, **770**, L32
 Hirota, T., Kim, M. K., Kurono, Y., & Honma, M. 2014, *ApJL*, **782**, L28
 Hirota, T., Machida, M. N., Matsushita, Y., et al. 2017, *NatAs*, **1**, 0146
 Issaoun, S., Goddi, C., Matthews, L. D., et al. 2017, *A&A*, **606**, A126
 Kim, M. K., Hirota, T., Honma, M., et al. 2008, *PASJ*, **60**, 991
 Kim, M. K., Hirota, T., Machida, M. N., et al. 2019, *ApJ*, **872**, 64
 Kounkel, M., Covey, K., Suárez, G., Román-Zúñiga, C., et al. 2018, *AJ*, **156**, 84
 Lenzuni, P., Gail, H.-P., & Henning, T. 1995, *ApJ*, **447**, 848
 Matthews, L. D., Greenhill, L. J., Goddi, C., et al. 2010, *ApJ*, **708**, 80
 Menten, K. M., Reid, M. J., Forbrich, J., & Brunthaler, A. 2007, *A&A*, **474**, 515
 Moeckel, N., & Goddi, C. 2012, *MNRAS*, **419**, 1390
 Niederhofer, F., Humphreys, E. M. L., & Goddi, C. 2012, *A&A*, **548**, A69
 Pineau des Forets, G., Roueff, E., Schilke, P., & Flower, D. R. 1993, *MNRAS*, **262**, 915
 Plambeck, R. L., & Wright, M. C. H. 2016, *ApJ*, **833**, 219
 Plambeck, R. L., Wright, M. C. H., Friedel, D. N., et al. 2009, *ApJL*, **704**, L25
 Podio, L., Codella, C., Lefloch, B., et al. 2017, *MNRAS: Lett.*, **470**, L16
 Reid, M. J., Menten, K. M., Greenhill, L. J., & Chandler, C. J. 2007, *ApJ*, **664**, 950
 Rodríguez, L. F., Poveda, A., Lizano, S., & Allen, C. 2005, *ApJL*, **627**, L65
 Sault, R. J., Teuben, P. J., & Wright, M. C. H. 1995, in ASP Conf. Ser. 77, *Astronomical Data Analysis Software and Systems IV*, ed. R. A. Shaw, H. E. Payne, & J. J. E. Hayes (San Francisco, CA: ASP), 433
 Schilke, P., Walmsley, C. M., Pineau des Forets, G., & Flower, D. R. 1997, *A&A*, **321**, 293
 Tachibana, S., Kamizuka, T., Hirota, T., et al. 2019, *ApJL*, **875**, L29
 Vaidya, B., & Goddi, C. 2013, *MNRAS: Lett.*, **429**, L50
 Wright, M. C. H., & Plambeck, R. L. 2017, *ApJ*, **843**, 83
 Wright, M. C. H., Plambeck, R. L., & Wilner, D. J. 1996, *ApJ*, **469**, 216
 Zanchet, A., Roncero, O., Agúndez, M., & Cernicharo, J. 2018, *ApJ*, **862**, 38